Tilted precession bands in ^{135}Nd

B. F. Lv,[1] C. M. Petrache [2,*] E. A. Lawrie,[3,4] A. Astier,[2] E. Dupont,[2] K. K. Zheng,[1,2] P. Greenlees,[5] H. Badran,[5]
T. Calverley,[5,6] D. M. Cox,[5,†] T. Grahn,[5] J. Hilton,[5,6] R. Julin,[5] S. Juutinen,[5] J. Konki,[5,‡] J. Pakarinen,[5] P. Papadakis,[5,§]
J. Partanen,[5] P. Rahkila,[5] P. Ruotsalainen,[5] M. Sandzelius,[5] J. Saren,[5] C. Scholey,[5] J. Sorri,[5,7] S. Stolze,[5,∥] J. Uusitalo,[5]
B. Cederwall,[8] A. Ertoprak,[8] H. Liu,[8] S. Guo,[1] J. G. Wang,[1] H. J. Ong,[1] X. H. Zhou,[1] Z. Y. Sun,[1] I. Kuti,[9] J. Timár,[9]
A. Tucholski,[10] J. Srebrny,[10] and C. Andreoiu[11]

[1]*Institute of Modern Physics, Chinese Academy of Sciences, Lanzhou 730000, China*
[2]*Université Paris-Saclay, CNRS/IN2P3, IJC Lab, 91405 Orsay, France*
[3]*iThemba Labs, National Research Foundation, PO Box 722, Somerset West 7129, South Africa*
[4]*Department of Physics, University of the Western Cape, Private Bag X17, 7535 Bellville, South Africa*
[5]*Department of Physics, University of Jyväskylä, Jyväskylä FIN-40014, Finland*
[6]*Department of Physics, University of Liverpool, The Oliver Lodge Laboratory, Liverpool L69 7ZE, United Kingdom*
[7]*Sodankylä Geophysical Observatory, University of Oulu, FIN-99600 Sodankylä, Finland*
[8]*KTH Department of Physics, S-10691 Stockholm, Sweden*
[9]*Institute for Nuclear Research (Atomki), Pf. 51, 4001 Debrecen, Hungary*
[10]*University of Warsaw, Heavy Ion Laboratory, Pasteura 5a, 02-093 Warsaw, Poland*
[11]*Department of Chemistry, Simon Fraser University, Burnaby, British Columbia V5A 1S6, Canada*

Two new excited bands built on the $\pi h_{11/2}$ configuration have been identified in ^{135}Nd in addition to the known $\pi h_{11/2}$ band. The energy spectra of the excited bands and the available electromagnetic transition probabilities are in good agreement with theoretical results obtained using quasiparticle-plus-triaxial-rotor model calculations. The properties of the bands identify them as tilted precession bands instead of wobbling bands. Our results give a new insight into the interpretation of the low-lying bands in odd-*A* mass nuclei, and can stimulate future studies to address the nuclear triaxiality.

I. INTRODUCTION

Atomic nuclei are finite quantum many-body systems which exhibit a large variety of shapes. In the $A \approx 130$ mass region, experimental and theoretical studies showed that the nuclei can have prolate, oblate, and triaxial shapes which are characterized by the deformation parameters (ε_2, γ) [1]. This is one of the best regions in the nuclear landscape to investigate shape coexistence and shape evolution over extended spin ranges. In particular, the nuclei with $Z \approx 60$, $N \approx 76$ are predicted by the macroscopic-microscopic finite-range liquid-drop model as an island of axial asymmetry on the nuclear chart [1]. Over the last decade many efforts were devoted to experimentally confirm the predicted nuclear triaxiality. Stable triaxial shapes are uniquely related to chiral and wobbling modes of excitations.

Nuclear chirality [2] has been intensively studied, and many chiral nuclei have been identified in the $A \approx 130$ mass region (e.g., ^{131}Ba [3], ^{133}La [4], ^{133}Ce [5], ^{135,136,137,138}Nd [6–11], ^{124,126,128,130}Cs [12–16]), as well as in the $A \approx 190$ mass region (e.g., ^{193,194,195,198}Tl [17–22]), in the $A \approx 100$ mass region (e.g., ^{103,105,111,113}Rh [23–26], ^{105,107}Ag [27,28]), and in the $A \approx 80$ mass region (e.g., ^{78,80}Br [29,30]), making this motion a more common phenomenon. For a recent review on chirality over the nuclear chart see Ref. [31].

Wobbling motion was initially proposed by Bohr and Mottelson for even-even nuclei [32]. It is a collective excitation mode that occurs when the three principal axes of the nuclear density distribution are unequal. The mode describes a nucleus rotating about the nuclear axis with the largest moment of inertia and the total angular momentum follows a precession trajectory around that axis. The associated energy spectra are a sequence of $\Delta I = 2$ rotational bands with increasing number of oscillation quanta. Each excited wobbling band corresponds to the excitation of an additional wobbling phonon with its energy and angular momentum. Recently, the wobbling motion has been been re-investigated by Frauendrof and Dönau [33], proposing the concepts of transverse and longitudinal wobbling motions in odd-mass nuclei, which are distinguished depending on whether the angular momentum of a high-*j* quasiparticle is oriented perpendicular or parallel

*Corresponding author: petrache@ijclab.in2p3.fr

[†]Present address: Department of Mathematical Physics, Lund Institute of Technology, S-22362 Lund, Sweden.

[‡]Present address: CERN, CH-1211 Geneva 23, Switzerland.

[§]Present address: Oliver Lodge Laboratory, University of Liverpool, Liverpool L69 7ZE, United Kingdom.

[∥]Present address: Physics Division, Argonne National Laboratory, Argonne, Illinois 60439, USA.

to the axis with largest moment of inertia (MoI), respectively. The expected characteristics of a transverse (longitudinal) wobbling band are (i) the $B[E2, I(n) \rightarrow I - 1(n - 1)]$ and $B[M1, I(n) \rightarrow I - 1(n - 1)]$ reduced transition probabilities are proportional to n, where n is the number of excited wobbling phonons and (ii) the wobbling energy decreases (increases) with increasing spin.

Experimentally, evidence for nuclear wobbling motion was reported in the $A \approx 160$ mass region: ^{161}Lu [34], ^{163}Lu [35,36], ^{165}Lu [37], ^{167}Lu [38], and ^{167}Ta [39]. In all these nuclei the wobbling bands with longitudinal coupling were assigned to the $\pi i_{13/2}$ configuration with large deformation of $\varepsilon_2 \approx 0.4$. The wobbling bands in the odd-mass Lu isotopes were recently reinterpreted as resulting from transverse wobbling [33]. In the $A \approx 100$ mass region, one-phonon transverse wobbling was reported in ^{105}Pd [40] built on the $\nu h_{11/2}$ configuration. In addition, in the $A \approx 130$ mass region, one-phonon and two-phonon transverse wobbling bands were reported in ^{135}Pr which are built on the $\pi h_{11/2}$ configuration with $\varepsilon_2 \approx 0.16$ and $\gamma \approx 26°$ deformation [33,41,42]. Transverse wobbling was firstly identified in the two-quasiparticle bands of the even-even nucleus ^{130}Ba [43], while longitudinal wobbling has been identified in ^{133}La [44]. However, the interpretation of the low-lying rotational bands in ^{135}Pr as one-phonon transverse wobbling has been seriously questioned by Tanabe *et al.* in Refs. [45,46] and therefore remains unclear. The experimental evidence for longitudinal wobbling is also reported in ^{187}Au [47] very recently, but the polarization measurement is not performed for the $\Delta I = 1$ interconnecting transitions and therefore the wobbling interpretation is not solid.

Very recently, Lawrie *et al.*, also questioned the wobbling interpretation of the low-lying yrare bands in odd-mass nuclei [48]. It was shown that the transverse wobbling equations as given in Ref. [33], are derived within a frozen harmonic approximation of the rotational Hamiltonian, and are therefore not equivalent to it. The three-dimensional rotation can be visualized as a precession of the total angular momentum around a certain axis, thus the name of tilted precession (TiP) bands was proposed for the quasiparticle-triaxial-rotor (QTR) bands in triaxial nuclei [48]. Therefore TiP bands for zero- and one-quasiparticle bands can be approximated with wobbling motion only when the approximation condition is valid, which occurs for at high spins and if (in the latter case) the angular momentum of the odd nucleon has longitudinal coupling.

This article is devoted to the observation of low-lying yrare bands in an even-odd nucleus. Three rotational bands of $h_{11/2}$ nature were identified in ^{135}Nd. The bands correspond to transverse coupling of the angular momenta of the odd neutron and the core. As all bands have $\Delta I = 1$ type, their angular momenta are generated by increasing the rotation along the intermediate axis, $R_\parallel$, mainly. This mode of angular momentum generation is incompatible with a possible interpretation of the bands in terms of transverse wobbling, because these wobbling bands are created by increasing the rotational angular momentum along the perpendicular axis, $R_\perp$, which creates bands of $\Delta I = 2$ type. The bands in ^{135}Nd are also incompatible with a possible interpretation in terms of longitudinal wobbling, because for these bands the odd

nucleon is aligned along the intermediate axis, along which the collective rotation $R_\parallel$ is dominant, giving rise to bands with $\Delta I = 2$ nature. Therefore in this work we interpret the observed $\Delta I = 1$ bands in ^{135}Nd using the QTR model in terms of tilted precession bands.

Within the QTR model rotational bands in odd-mass nuclei are built by a coupling of the single-particle angular momentum of the odd nucleon and the angular momentum of the rotating even-even core. We will discuss the case of transverse coupling of the angular momenta of the odd nucleon and of the rotating core, in which they are orthogonal to each other. In axially symmetric nuclei, this coupling produces deformation-aligned $\Delta I = 1$ bands above the band-head levels with $I = K = \Omega$ (where I, K, and Ω are the total angular momentum, its projection, and the projection of the single-particle angular momentum on the symmetry axis, respectively). For triaxial nuclei both K and Ω projections are not conserved, but for $\gamma = 30°$ and an odd nucleon in the $h_{11/2}$ or $i_{13/2}$ shells, it was shown that K and Ω are approximately good [49].

For triaxial nuclei, in addition to the rotation along the intermediate axis, rotating along the short and long axes are also possible. In Fig. 1, we denote with $R_\parallel$ the rotation around the intermediate axis, while rotation around the orthogonal axis (long or short) is labeled as $R_\perp$. The yrast band shown in Fig. 1(a) in black will be the only band observed for such a coupling if the nuclear shape is axially symmetric. Additional bands (shown in blue and red) come down in energy for triaxial shapes. Each band corresponds to an increase in $R_\parallel$, while each excited band is generated by an extra $\approx 2\hbar$ in $R_\perp$. The orientation of the total angular momentum I for the yrast band is illustrated in Fig. 1(b) as black arrows connected with dotted black line. The states in the yrast band correspond to $K_\perp = \Omega_\perp = 9/2$, and are thus labeled by $[K_\perp]$, as belonging to the [9/2] band. The generation of the angular momentum in the first excited band is illustrated in Fig. 1(b) by the arrows in blue connected by dotted blue line. This excited band also represents generation of angular momentum mostly along the intermediate axis, but it corresponds to a collective rotation along the orthogonal axis with $R_\perp \approx 2\hbar$. Thus, the band has $K_\perp = 13/2$ and is labeled by [13/2] in Figs. 1(a) and 1(b). Similarly, the second excited band illustrated in red in Figs. 1(a) and 1(b) corresponds to $K_\perp = 17/2$, and is labeled as [17/2]. Note that all bands have $\Delta I = 1$ nature, and that the band-head spin of each excited band increases by $2\hbar$.

In some nuclei the excited [13/2] and [17/2] bands come so low in energy that the 13/2 state of the [13/2] band lies lower in energy than the 13/2 state of the [9/2] band, and the 17/2 state of the [17/2] band lies at lower energy than the 17/2 states of the [9/2] and [13/2] bands. This may happen due to the Coriolis interaction which lowers the energy of the states for which the rotational and single-particle angular momenta point in similar directions, for instance, for the 13/2 state of the [13/2] band. Therefore the yrast line includes the 9/2 state of the [9/2] band, the 13/2 state of the [13/2] band, and the 17/2 state of the [17/2] band, as show in Fig. 1(c). All levels in this band correspond to states for which the collective rotation is mainly around the perpendicular axis. Therefore the angular momentum along the band is generated by increasing $R_\perp$. All states have $I = I_\perp$, and the band can be labeled by
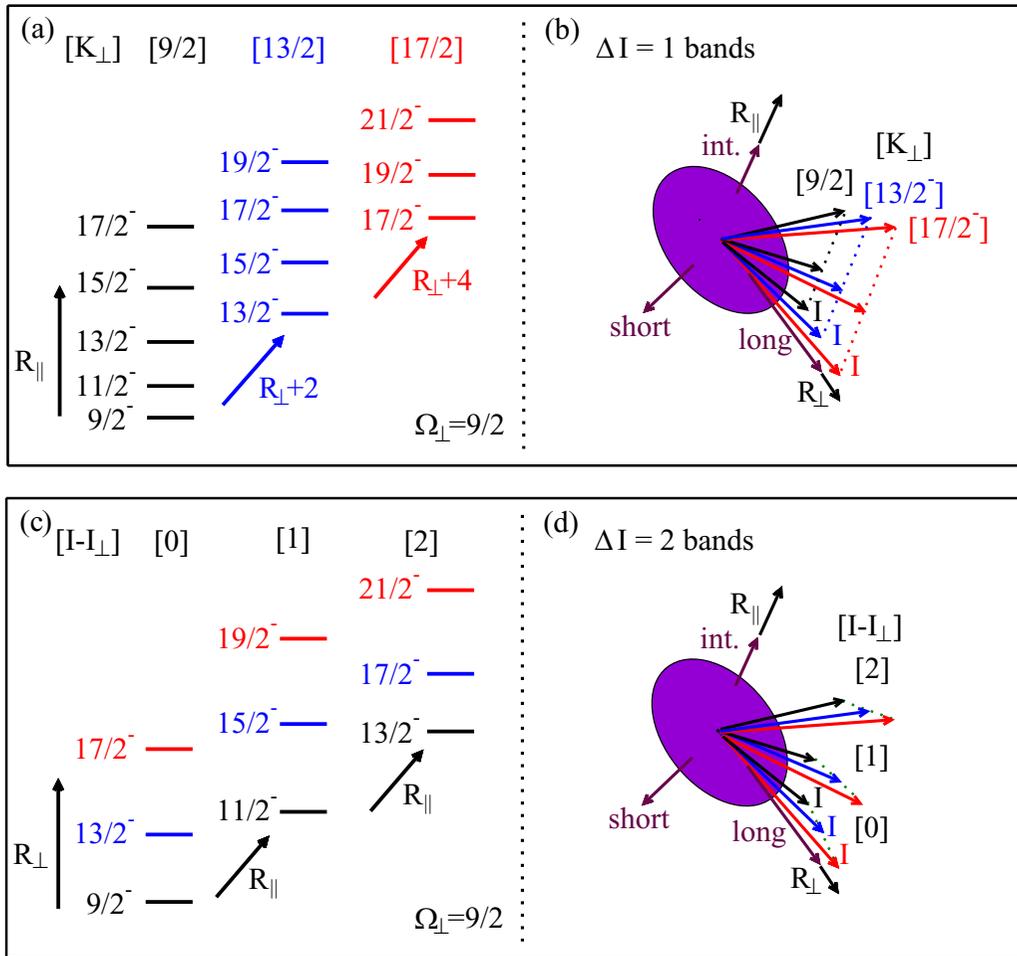
FIG. 1. (a) and (b) illustrate rotational bands and the angular momentum generation, respectively, in odd-mass triaxial nuclei with $\Delta I = 1$ nature and $\Omega = 9/2$. (c) and (d) represent such bands with $\Delta I = 2$ nature. The $\Delta I = 1$ bands are labeled by $[K_\perp]$, while the $\Delta I = 2$ bands by $[I - I_\perp]$. The symbols $\parallel$ and $\perp$ denote projections along the intermediate axis (the axis with largest MoI) and orthogonal to it (on the long or short axis), respectively. For more information see text.

$[I - I_\perp]$, and the lowest band is therefore called band [0]. The angular momenta of the [0] band are illustrated in Fig. 1(d) by the dotted green line. Each excited band corresponds to generating angular momentum in a similar way, that is by increasing $R_\perp$ along the band, but they also involve an increase in $R_\parallel$. Note that these bands have $\Delta I = 2$ nature and that each exited band has opposite signature.

Each one of the bands illustrated in panels (b) and (d) of Fig. 1 represents a precession in a semiclassical way of the total angular momentum. One can visualize the trajectory of the precession of the total angular momentum as the intersection of the angular momentum sphere and the energy ellipsoid as proposed in Ref. [33]. The precession of the total angular momentum for the yrast $\Delta I = 1$ and $\Delta I = 2$ bands is illustrated in Fig. 2.

The yrast $\Delta I = 1$ band, labeled as [9/2] in Figs. 1(a) and 1(b), is illustrated in panels (a)–(c) of Fig. 2. The band-head level shown in panel (a) corresponds to a precession of I along the perpendicular axis. The angular momentum of this state, mostly due to the single-particle angular momentum, is aligned along the perpendicular axis. The higher-spin states in

the [9/2] $\Delta I = 1$ band are produced by increasing the rotation along the intermediate axis, $R_\parallel$, which tilts the total angular momentum towards the intermediate axis. As $R_\parallel$ increases, the tilt of I also increases, moving the direction of the total angular momentum towards the intermediate axis, see panels (b) and (c) of Fig. 2. The rotational band is of $\Delta I = 1$ type.

Panels (d)–(f) of Fig. 2 illustrate the precession for the yrast $\Delta I = 2$ band, denoted as [0] band in Figs. 1(c) and 1(d). The angular momentum in this band is generated by the increase of $R_\perp$, therefore even at high spins the total angular momentum still precesses along the perpendicular axis, as shown in panels (d) and (e) of Fig. 2. The band is of $\Delta I = 2$ type, as the rotational and the single-particle angular momenta are aligned. The excited bands would correspond to similar precession and have alternating signatures. There is however a critical spin, I_c, beyond which the precession of the total angular momentum moves away from the perpendicular axis, as shown in panel (f) of Fig. 2. For spins beyond I_c each pair of $\Delta I = 2$ bands with opposite signature [e.g., bands [0] and [1] in Figs. 1(c) and 1(d)] become degenerate in energy, forming a $\Delta I = 1$ band, see Fig. 13(e) of the Appendix and Ref. [48]. Should
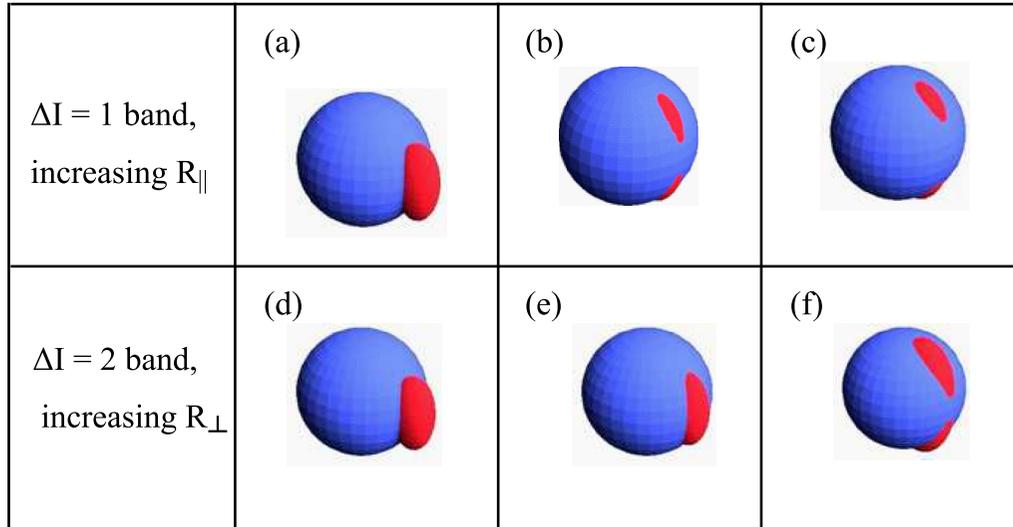
FIG. 2. Schematic illustration of the trajectory of the total angular momentum for transverse coupling of the angular momenta of the valence nucleon and the core. The total angular momentum trajectory is the intersection of the angular momentum sphere (in blue) and the energy ellipsoid (in red). (a)–(c) correspond to the yrast $\Delta I = 1$ band as the spin I increases due to rotation mainly along the intermediate axis. (d)–(f) correspond to the yrast $\Delta I = 2$ band as the spin I increases due to rotation mainly along the long (or short) axis.

the value of I_c, which depends on the MoI along the three axes and the single-particle angular momentum, be similar to the band-head spin, one cannot generate bands of $\Delta I = 2$ type, and the angular momentum generation proceeds mainly along the intermediate axis producing bands of $\Delta I = 1$ type. Thus for transverse coupling, bands of $\Delta I = 2$ type can be observed at best in a limited spin range.

Therefore odd-mass nuclei with transverse orientation of the angular momenta of the valence nucleon and of the rotating core may show rotational bands of either $\Delta I = 2$ or $\Delta I = 1$ type depending on the value of the critical spin I_c. Bands of $\Delta I = 2$ type can be observed in a limited spin range below I_c. It had been proposed that the $\Delta I = 2$ bands associated with transverse coupling in triaxial nuclei can be approximated as transverse wobbling bands [33] (for more details see the Appendix).

In this article, the experimental details and results are presented in Sec. II. In Sec. III, the experimental results are compared with theoretical calculations. This is followed by a summary of the present work in Sec. IV.

II. EXPERIMENTAL DETAILS AND RESULTS

Low-lying states in ^{135}Nd were populated using the ^{100}Mo(^{40}Ar, 5n) reaction. The ^{40}Ar beam with an energy of 152 MeV was provided by the K130 Cyclotron at the University of Jyväskylä, Finland. We used as target a self-supported enriched ^{100}Mo foil of 0.5 mg/cm^2 thickness. The emitted γ rays were detected by the JUROGAM II spectrometer equipped with 39 Compton suppressed Ge detectors in which 15 tapered detectors are placed at backward angles and 24 Clover detectors are placed around 90° relative to the beam direction. Data were acquired by the triggerless total data readout (TDR) data system and the events were time-stamped using a 100 MHz clock [51]. Details of the experimental setup can also be found in Ref. [52]. A total of 5.1×10^{10} three

and higher-fold γ-ray coincidence events were obtained and stored. Energy and efficiency calibrations were performed for each detector of the JUROGAM II array using standard ^{152}Eu and ^{133}Ba radioactive sources. The calibrated data were then sorted into coincidence γ-γ matrices and γ-γ-γ cubes, and analyzed using the RADWARE software [53,54].

The partial level scheme of ^{135}Nd showing the previously known D1 and newly identified bands TiP1 and TiP2 (in red) is plotted in Fig. 3. Spectra showing the newly identified transitions in bands TiP1 and TiP2 are given in Fig. 4. The level scheme is constructed on the basis of the relative intensity (I_γ) balance, coincidence relationships of the γ-ray transitions obtained from the analysis of double- and triple-gated spectra. The multipolarity of the γ-ray transitions were obtained using the directional correlation from oriented states (DCO) ratios (R_{DCO}) and two-point angular correlation (anisotropy) ratios R_{ac} [55,56]. Detailed experimental information on levels and γ-ray transitions is presented in Table I.
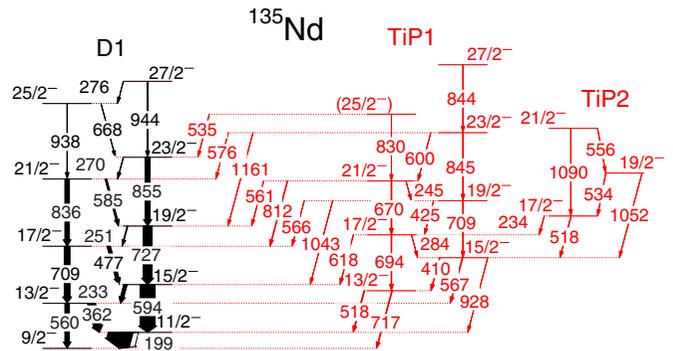

FIG. 3. Partial level scheme of ^{135}Nd relevant for the present work. Known (new) levels and transitions are drawn with black (red) colors, respectively.
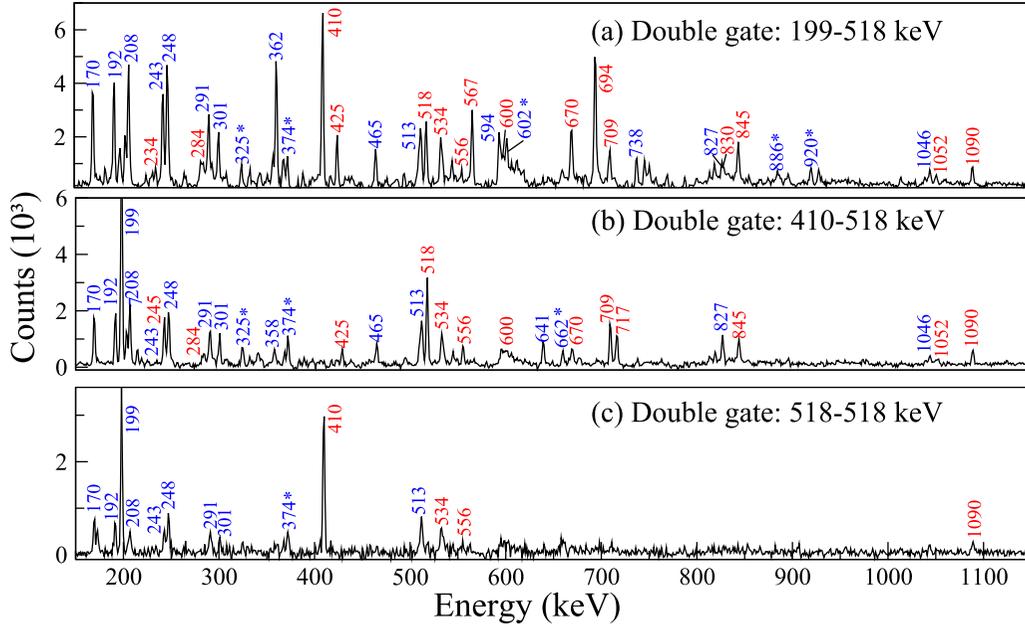
FIG. 4. Spectra for the bands TiP1 and TiP2 of ^{135}Nd showing the newly identified transitions (in red color). The peaks marked with an asterisk are contaminants from ^{136}Nd.

To extract the R_{DCO} values, the data were sorted into an asymmetric γ-γ matrix constructed by sorting prompt coincidence events with the tapered detectors mounted at $157.6°$ on one axis and clover detectors around $90°$ ($75.5°$ and $104.5°$) on the other axis. Then, the R_{DCO} ratio was calculated using the extracted relative intensities of the γ rays (I_γ) from these spectra, normalized by the different efficiencies of the two sets of detectors. The relation is written as

$$R_{\text{DCO}} = \frac{I_\gamma(157.6°, \text{ gated on } \approx 90°)}{I_\gamma(\approx 90°, \text{ gated on } 157.6°)}. \quad (1)$$

The R_{DCO} values obtained by gating on a stretched quadrupole transition are ≈ 1 for stretched quadrupole and ≈ 0.46 for dipole transitions, while those obtained by gating on a stretched dipole transition are ≈ 1 for a dipole and ≈ 2.1 for a quadrupole transition.

The values of R_{ac} were extracted from two γ-γ matrices, one having γ rays detected by tapered detectors at ($157.6°$ and $133.6°$) on one axis and all detectors on the other axis, and another matrix having γ rays detected by clover detectors around $90°$ ($75.5°$ and $104.5°$) on one axis and all detectors on the other axis. The same energy gates on the axis of all detectors were put in both matrices, and gated spectra were projected on the other axis. The R_{ac} was calculated by

$$R_{ac} = \frac{I_\gamma(157.6° + 133.6°, \text{ gated on all angles})}{I_\gamma(\approx 90°, \text{ gated on all angles})}. \quad (2)$$

The R_{ac} values for stretched dipole and quadrupole transitions are 0.8 and 1.4, respectively, have been deduced from the analysis of strong $E2$, $E1$, and $M1$ transitions of ^{136}Nd [52]. Note that this method is very useful particularly for weak transitions, for which the statistics is not sufficient to extract DCO ratios.

In order to firmly establish the parity of the newly identified bands, linear polarization measurements were performed for a few clean, strong, linking γ-ray transitions as described in Refs. [57,58]. In the present work, two matrices were constructed with events in which γ rays were scattered between the crystals of a clover detector in parallel (perpendicular) directions relative to the beam direction on one axis, and γ rays detected by all detectors on the other axis. The polarization asymmetry is defined by

$$A_P = \frac{a(E_\gamma)N_\perp - N_\parallel}{a(E_\gamma)N_\perp + N_\parallel}, \quad (3)$$

where $N_\perp$ and $N_\parallel$ are the number of coincidence counts for a γ ray of interest obtained by setting the same gates in the two asymmetric matrices on the all-detector axis. The $a(E_\gamma)$ is the normalization factor due to the asymmetry in the response of the perpendicular and parallel events for clovers. The variation of $a(E_\gamma)$ for JUROGAM II clovers can be found in Ref. [57]. The typical A_P values for pure stretched electric and pure stretched magnetic transitions are around 0.1 and -0.1, respectively. Figure 5 shows examples of polarization spectra. One can observe that the 727-keV ($19/2^- \rightarrow 15/2^-$) transition of band D1 exhibit a clear electric character, while the 518-keV ($13/2^- \rightarrow 11/2^-$) and 567-keV ($15/2^- \rightarrow 13/2^-$) transitions linking band TiP1 and D1 exhibit different nature. It should be mentioned that the perpendicular spectra were normalized by the $a(E_\gamma)$ in Fig 5.

Band D1 was previously reported in Refs. [6,7,50] with spin-parity values firmly assigned to all states. In the present work, we mainly focus on the measurement of the mixing ratios δ of the $\Delta I = 1$ transitions by using angular distribution analysis procedures described in Refs. [41,43]. The δ values of the 362-, 233-, and 477-keV transitions of band D1 are

TABLE I. Experimental information including the γ-ray energies, energies of the initial levels E_i, intensities I_γ, R_{DCO}, and/or R_{ac}, multipolarities, and the spin-parity assignments to the observed states in ^{135}Nd.

γ-ray energy[a]	E_i (keV)	Intensity[b]	R_{DCO}[c]	R_{ac}[d]	Multipolarity	$J_i^\pi \rightarrow J_f^\pi$
Band TiP1						
284.3	1411.2	0.35(5)	0.55(8)[e]		$M1/E2$	$17/2^- \rightarrow 15/2^-$
245.1	2081.3	0.18(3)		0.91(24)	$M1/E2$	$21/2^- \rightarrow 19/2^-$
410.2	1127.1	2.9(3)	0.88(10)[e]		$M1/E2$	$15/2^- \rightarrow 13/2^-$
424.9	1836.0	0.75(6)		0.69(12)	$M1$	$19/2^- \rightarrow 17/2^-$
599.9	2681.0	0.9(2)				$23/2^- \rightarrow 21/2^-$
670.1	2081.3	3.1(5)	1.06(24)[e]		$E2$	$21/2^- \rightarrow 17/2^-$
694.3	1411.2	2.6(4)	0.98(13)[e]		$E2$	$17/2^- \rightarrow 13/2^-$
708.9	1836.0	2.4(6)		1.41(15)	$E2$	$19/2^- \rightarrow 15/2^-$
829.9	2911.0	0.18(10)				$(25/2^-) \rightarrow 21/2^-$
844.1	3525.1	1.5(2)		1.32(15)	$E2$	$27/2^- \rightarrow 23/2^-$
845.0	2681.0	2.2(6)		1.4(3)	$E2$	$23/2^- \rightarrow 19/2^-$
518.1	716.9	3.7(4)	0.69(8)[e]		$M1/E2$	$13/2^- \rightarrow 11/2^-$
535.1	2911.0	0.10(6)				$(25/2^-) \rightarrow 23/2^-$
560.7	2081.3	1.1(4)	0.8(2)[e]		$M1/E2$	$21/2^- \rightarrow 19/2^-$
566.0	1836.0	0.9(2)		0.54(17)	$M1/E2$	$19/2^- \rightarrow 17/2^-$
566.8	1127.1	3.2(5)	0.36(6)[e]		$M1/E2$	$15/2^- \rightarrow 13/2^-$
575.9	2681.0	0.15(7)	0.72(6)[e]		$M1/E2$	$23/2^- \rightarrow 21/2^-$
618.3	1411.2	1.7(2)	0.83(10)[e]		$M1/E2$	$17/2^- \rightarrow 15/2^-$
717.1	716.9	3.0(3)	1.26(32)[e]		$E2$	$13/2^- \rightarrow 9/2^-$
811.6	2081.3	2.5(2)	1.10(12)[e]		$E2$	$21/2^- \rightarrow 17/2^-$
928.0	1127.1	0.15(5)				$15/2^- \rightarrow 11/2^-$
1043.1	1836.0	0.12(4)				$19/2^- \rightarrow 15/2^-$
1160.9	2681.0	0.4(1)				$23/2^- \rightarrow 19/2^-$
Band TiP2						
533.8	2179.0	0.7(1)		1.07(17)	$M1/E2$	$19/2^- \rightarrow 17/2^-$
556.4	2735.0	0.11(2)				$21/2^- \rightarrow 19/2^-$
1089.6	2735.0	0.65(9)		1.25(33)	$E2$	$21/2^- \rightarrow 17/2^-$
234.0	1645.4	0.12(4)				$17/2^- \rightarrow 17/2^-$
518.3	1645.4	1.9(2)		1.05(13)	$M1/E2$	$17/2^- \rightarrow 15/2^-$
1051.8	2179.0	0.25(3)		1.29(31)	$E2$	$19/2^- \rightarrow 15/2^-$

[a]The error on the transition energies is 0.2 keV for transitions below 1000 keV of the ^{135}Nd reaction channel, 0.5 keV for transitions above 1000 keV and 1 keV for transitions above 1200 keV.

[b]Relative intensities corrected for efficiency, normalized to the intensity of the 198.8 keV transition. The transition intensities were obtained from a combination of total projection and gated spectra.

[c]R_{DCO} has been deduced from asymmetric γ-γ coincidence matrix sorted with detectors at 157.6° on one axis, and detectors at ≈90° on the other axis. The tentative spin - parity of the states are given in parenthesis.

[d]R_{ac} has been deduced from two asymmetric γ-γ coincidence matrices sorted with detectors at 133.6° and 157.6° on one axis, and detectors at ≈90° on the other axis, respectively. The tentative spin-parity of the states are given in parenthesis.

[e]DCO ratio from spectrum gated on stretched quadrupole transition.

$-0.16(7)$, $-0.08(2)$, and $-0.13(5)$, respectively. The present values of the mixing ratios of these in-band $M1/E2$ transitions are in good agreement with the values reported in Ref. [50]. It should be pointed out that the mixing ratio of the weak 251-keV transition is taken from Ref. [50], since in the present data it is strongly contaminated by the 248-keV transition in the high-spin of band D5 (see Ref. [7]).

Band TiP1 is a completely new band which decays to band D1 via the 518-, 618-, 566-, 561-, 576-, and 535-keV $\Delta I = 1$ transitions, and the 717-, 1043-, 812-, and 1161-keV $E2$ transitions. The extracted R_{DCO} and linear polarization values for the 518-keV ($13/2^- \rightarrow 11/2^-$) transition, and those of the 717- and 812-keV transitions which have $E2$ character, fix the spin and parity of band-head of TiP1 at $I^\pi = 13/2^-$ (see Table I). To understand the nature of the transitions linking band TiP1 with the band D1, the R_{DCO}, linear polarization, and mixing ratio δ were extracted for the transitions with sufficient intensity. It should be mentioned that for wobbling bands, the linking transitions are $\Delta I = 1$ with predominant $E2$ character [33]. As one can see in Tables I and II, the measured R_{DCO} and linear polarization values for the 618- and 566-keV transitions, the connecting transitions between the band TiP1 and D1, are clearly $\Delta I = 1$, predominantly $M1$ in nature. Also, based on the angular distribution measurements for the 618- and 566-keV transitions, the extracted mixing ratios δ are 0.32(5) and 0.33(9), respectively, which suggests relatively small $E2$ component. Figure 6 shows typical angular distribution fit for the transitions linking band TiP1 and band D1, and the resulting δ values are listed in Table II .
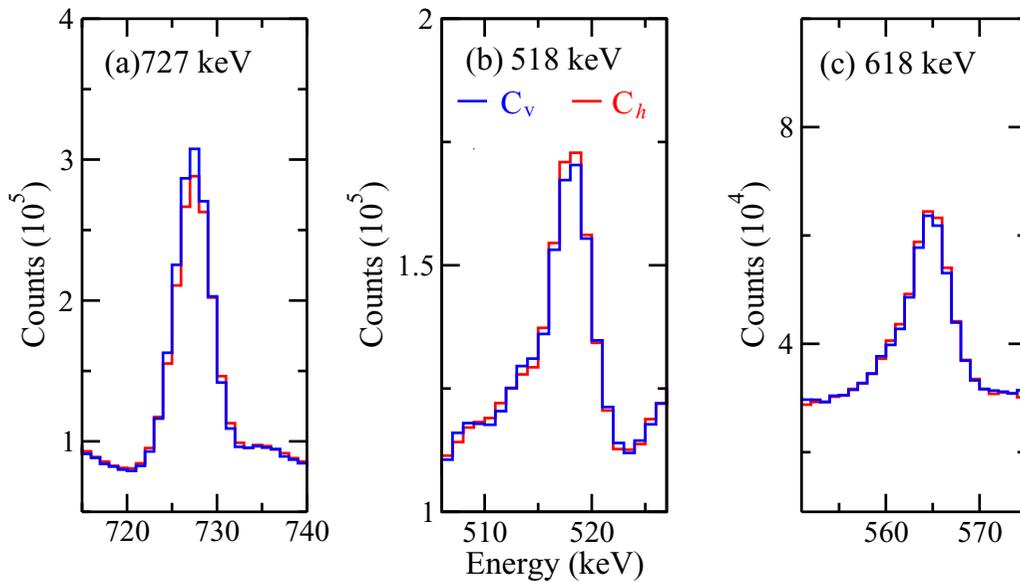
FIG. 5. Polarization spectra measured for the 727-keV, 518-keV ($13/2^- \to 11/2^-$), and 618-keV transitions in which the perpendicular (C_V) and parallel (C_h) spectra are marked with blue and red colors, respectively.

Band TiP2 consisting of three levels with spins from $17/2^-$ to $21/2^-$, interconnected by the 534- and 556-keV dipole transitions, is also newly identified. It decays to band TiP1 by three transitions of 234, 518, and 1052 keV. Figure 4 shows the newly identified in-band and out-of-band transitions of bands TiP2. As one can see in panel (b), by setting a double gate on the 410-518 keV cascade, all in-band and out-of-band transitions of band TiP2 are clearly visible. Note the existence of two 518-keV transitions in Fig. 3, one connecting band TiP1 to D1, and the other connecting band TiP2 to TiP1. How-

ever, as shown in panel (c), by double-gating on the 518-keV transitions, the 410-, 534-, 556-, and 1090-keV transitions are clearly observed, giving clear evidence for the assignment of the new band structure to ^{135}Nd. The spins of the levels in band TiP2 were established through the 1052- and 518-keV transitions of quadrupole and dipole character, respectively. By setting a gate on the 717-keV ($13/2^- \to 9/2^-$) transition in band TiP1, the polarization of the 518-keV ($17/2^- \to 15/2^-$) transition linking band TiP2 to TiP1 was extracted with large error bar: the value is $-0.14(8)$ and therefore

TABLE II. The experimental multipole mixing ratios δ, $E2$ fractions, asymmetries A_P, and the experimental reduced transition probability ratios for the in-band and connecting transitions of bands D1, TiP1, and TiP2.

Initial I^π	Final I^π	E_γ (keV)	δ	$E2$ fraction (%)	A_P	$B(M1)_{\text{out}}/B(E2)_{\text{in}}$	$B(E2)_{\text{out}}/B(E2)_{\text{in}}$
Band D1							
$\frac{13}{2}^-$	$\frac{11}{2}^-$	361.7	$-0.16(7)$	2.5 ± 2.1		1.3(12)	0.36(32)
$\frac{15}{2}^-$	$\frac{13}{2}^-$	232.6	$-0.08(2)$	0.6 ± 0.3		0.82(43)	0.14(7)
$\frac{17}{2}^-$	$\frac{15}{2}^-$	476.7	$-0.13(5)$	1.7 ± 1.3		0.66(52)	0.07(6)
$\frac{19}{2}^-$	$\frac{17}{2}^-$	250.6	$-0.19(8)^{\text{a}}$	3.5 ± 2.8		0.68(57)	0.56(47)
$\frac{19}{2}^-$	$\frac{15}{2}^-$	727.3			0.037(3)		
Band TiP1							
$\frac{13}{2}^-$	$\frac{11}{2}^-$	518.1	$-0.11(5)$	1.2 ± 1.1	$-0.024(10)$		
$\frac{15}{2}^-$	$\frac{13}{2}^-$	410.2	$-0.21(5)$	4.2 ± 1.9	$-0.070(18)$		
$\frac{15}{2}^-$	$\frac{13}{2}^-$	566.8	$-0.48(14)$	18.7 ± 8.9	$-0.019(6)$		
$\frac{17}{2}^-$	$\frac{15}{2}^-$	618.3	$-0.32(5)$	9.3 ± 2.6	$-0.012(4)$	0.28(10)	0.11(4)
$\frac{19}{2}^-$	$\frac{17}{2}^-$	566.0	$-0.33(9)$	9.8 ± 4.8	$-0.081(72)$	0.24(14)	0.12(7)
$\frac{21}{2}^-$	$\frac{19}{2}^-$	560.7	$-0.16(7)$	2.5 ± 2.1		0.18(17)	0.02(2)
$\frac{23}{2}^-$	$\frac{21}{2}^-$	575.9					
$\frac{21}{2}^-$	$\frac{17}{2}^-$	811.6			0.068(18)		
Band TiP2							
$\frac{17}{2}^-$	$\frac{15}{2}^-$	518.3	$-0.26(8)$	6.3 ± 3.6	$-0.14(8)$		

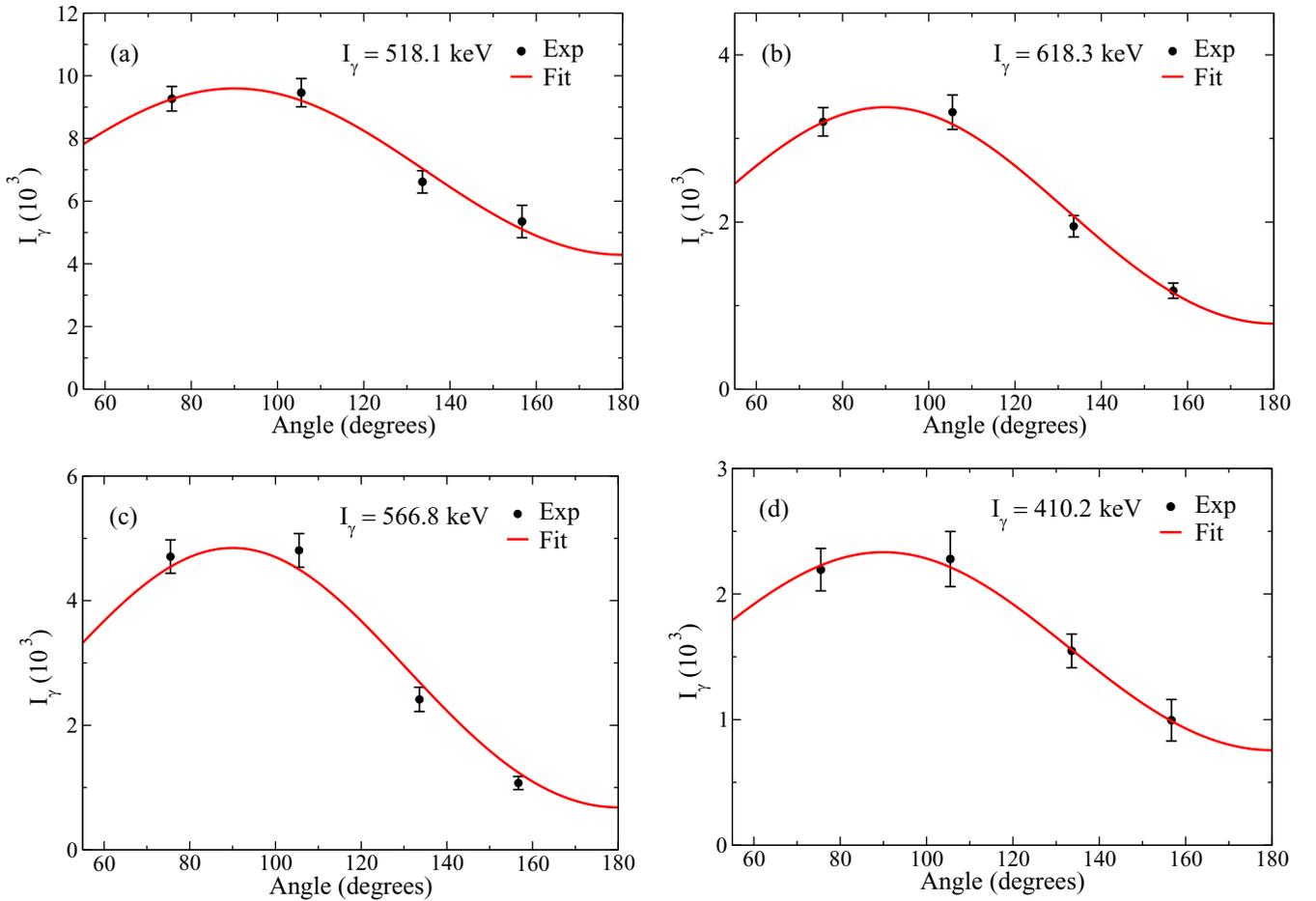$^{\text{a}}$Data were taken from Ref. [50].

FIG. 6. Angular distribution figures for the 518-, 618-, and 567-keV interconnecting transitions between the bands TiP1 and D1, and for the 410-keV transition of band TiP1. The angular distributions of the 518-, 618-, 567-, and 410-keV transitions were obtained by gating on the 694-, 594-, 709-, and 518-keV transitions, respectively.

has predominant magnetic character, fixing thus the negative-parity of band TiP2. To ascertain the nature of the 518-keV transition linking band TiP2 to band TiP1, its mixing ratio of $\delta = -0.26(8)$ was extracted. Note that both the polarization asymmetry measurement and the angular distribution analysis for the 518-keV ($17/2^- \rightarrow 15/2^-$) transition indicate its predominant $M1$ nature. The 234-keV transition is too weak for measuring its multipolarity and mixing ratio, however, the extracted R_{ac} for the 1052-keV transition is consistent with stretched quadrupole character, supporting the proposed spin and parity of the levels of TiP2.

III. DISCUSSION

In order to demonstrate the nature of the low-lying rotational bands in ^{135}Nd, the QTR model [59] was used. The MoI's of the core were assumed to follow the irrotational-flow dependence with respect to the γ deformation [60]. The spin dependence of the MoI's was parametrized using Harris parameters of $\mathcal{J}_0 = 5$ $\hbar^2 \mathrm{MeV}^{-1}$ and $\mathcal{J}_1 = 71.4$ $\hbar^4 \mathrm{MeV}^{-3}$. The Coriolis interaction was reduced by a factor of 0.7, as usually adopted in this mass region. The parameters for the electromagnetic transition probabilities were calculated with

an effective g_s factor of $g_s = 0.6 g_{\mathrm{free}}$, and the g factor for the core of $g_R = 0.44$ is adopted [61].

For an axially asymmetric shape the wave functions for the odd nucleon do not coincide with the Nilsson basis wave functions. The present calculations include the seven closest to the Fermi level negative-parity orbitals, listed in Table III. Each orbital has contributions from basis functions labeled with the shell from which they originate and the projection of the single-particle angular momentum on the long axis, Ω_l. The orbitals labeled #16–#19 have predominant (more than 75%) contribution from a $h_{11/2}$ orbital with a projection on the long axis of $\Omega_l = 5/2, 7/2, 9/2$, and $11/2$, respectively. The orbitals #20–#22 correspond to a mixture of many orbitals from the h and f shells.

As discussed in the introduction, the results of the QTR model for an odd-mass nucleus, can be described as follows:

(i) the states where the rotation increases mostly along the intermediate axis form rotational $\Delta I = 1$ bands as those shown in different colors in Fig. 7.

(ii) the increase of the rotational angular momentum with $|\Delta R| = 2\hbar$ along the long (or short) nuclear axis, gives rise to excited band-head states on top of which bands like those described at point (i) can develop.

TABLE III. The basis wave functions with contribution larger than 5%, labeled according to the shell from which they originate and their angular momentum projection on the long axis Ω_l for the seven negative-parity orbitals included in the calculations. The dominant Ω_l, corresponds to Ω_l of the basis wave function more than 75% contribution.

Orbital	Contributing basis functions	Ω_l
#16	76% ($h_{11/2}$, 5/2), 12% ($h_{11/2}$, 1/2), 5% ($f_{7/2}$, 1/2)	5/2
#17	90% ($h_{11/2}$, 7/2)	7/2
#18	96% ($h_{11/2}$, 9/2)	9/2
#19	96% ($h_{11/2}$, 11/2)	11/2
#20	49% ($f_{7/2}$, 1/2), 7% ($h_{11/2}$, 1/2), 8% ($h_{9/2}$, 1/2), 5% ($f_{5/2}$, 1/2), 15% ($p_{3/2}$, 1/2), 8% ($f_{7/2}$, 3/2)	−
#21	50% ($h_{9/2}$, 1/2), 9% ($f_{5/2}$, 1/2), 23% ($h_{9/2}$, 3/2), 7% ($f_{7/2}$, 3/2)	−
#22	37% ($f_{7/2}$, 3/2), 10% ($f_{7/2}$, 1/2), 7% ($p_{3/2}$, 1/2), 5% ($h_{11/2}$, 3/2), 10% ($h_{9/2}$, 3/2), 5% ($f_{5/2}$, 3/2)	−

The QTR model finds the neutron Fermi level in ^{135}Nd close to the $h_{11/2}$ orbital with projection $\Omega = 9/2$, but the $h_{11/2}$ orbital with $\Omega = 11/2$ is also involved in some of the yrare bands. Therefore each band in Fig. 7 is labeled by the corresponding Ω_l and K_l, [Ω_l, K_l]. One should keep in mind that the illustration shown in Fig. 7 is simplified, in general the states correspond to a mixture of contributions of different type.

Band D1 was assigned the $\nu(h_{11/2})^{-1}[514]\frac{9}{2}^-$ configuration and has been studied previously in Refs. [6,7,50,62]. The deformation parameters used in the present QTR calculations are $\beta = 0.19$ and $\gamma = 25°$, which are similar to those used in Ref. [63], and the same as in our recent work reported in Ref. [7], in which the measured transition probabilities and energy spectra of band D1 were well reproduced by constrained covariant density functional theory and particle rotor model (PRM) calculations. The newly identified TiP bands are also assigned to the $\nu(h_{11/2})^{-1}$ configuration, but with different R_l and Ω_l values. Figure 8 shows the experimental excitation energies in comparison with the results of QTR calculations for the D1 and TiP bands. The calculated excitation energies of the states in band D1 are in good agreement with the experimental data in the whole spin region. One shortcoming of the calculations is the predicted energy of the $11/2^-$ state which is very close to that of the $9/2^-$ state. This impacts

the excitation energy of the high-spin states too, causing some under-prediction of their excitation energies.

Figure 9 provides the wave functions for the states of band D1, where the contributions from the basis functions corresponding to the single-particle orbital with a given number (the four bins along the x axis for each state based on orbitals #16–#19, respectively, see Table III) and the projection of the total angular momentum on the long axis, K_l on the y axis of the plot (see the legend), are shown for each state of the band with $I = 9/2^-$ to $27/2^-$. For instance, the $9/2^-$ state has almost 80% contribution from the basis function (#18, $K_l = 9/2$), shown as purple column in Fig. 9, which corresponds to a dominant $h_{11/2}[514]9/2$ single-particle contribution and $K_l = \Omega_l = 9/2$. This level therefore has a dominant [9/2, 9/2] nature, see Fig. 7. The yellow column corresponds to a small (approximately 10%) contribution from the basis function #17 (with mainly $\nu h_{11/2}[523]\frac{7}{2}$ nature), which reflects a $h_{11/2}$ orbital with $\Omega_l = 7/2$ and suggests the presence of a small misalignment of the single-particle angular momentum away from the long axis. The wave function for the $11/2^-$ state of D1 also has a dominant contribution from the basis state #18 and $K_l = 9/2$, but also a considerable contribution from the basis function #19 with $K_l = 11/2$. At higher spins, the wave functions of the states still contain largest contribu-
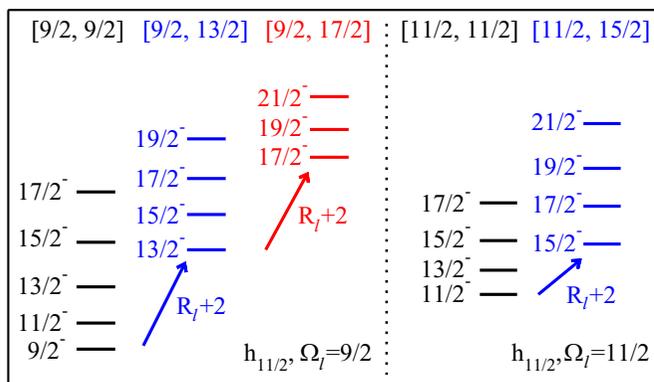

FIG. 7. Sketch of the TiP bands, based on the $h_{11/2}$ orbitals with projections on the long nuclear axis of $\Omega_l = 9/2$ (left), and $\Omega_l = 11/2$ (right), for a Fermi level closer to the $\Omega_l = 9/2$ orbital. Each TiP band is labeled with [Ω_l, K_l].
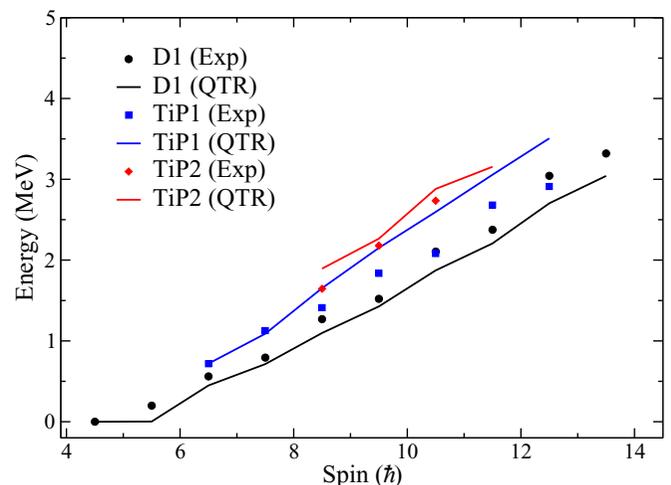

FIG. 8. Calculated excitation energies for the D1 and the TiP bands in ^{135}Nd in comparison with experimental data.
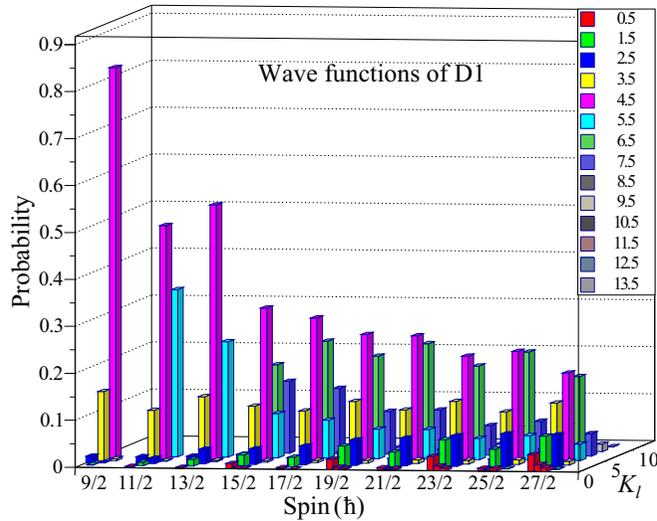
FIG. 9. Contributions of the basis wave functions labeled with their $h_{11/2}$ singe-particle orbitals and projections K_l on the long axis for the states with $I = 9/2$ to $27/2$ of D1 band in ^{135}Nd. The color corresponds to K_l, as shown in the legend.

tion from the basis state #18, however, there are often other contributions too, for instance a contribution from the basis state #18 but with $K_l = 13/2$. There are also many contributions from basis functions #16 and #17 with lower Ω_l, which represents Coriolis misalignment of the odd neutron.

One can also observe in Fig. 8 that the calculated excitation energies for TiP1 are in good agreement with the experimental data for the lowest states with spin $I = 13/2$ and $I = 15/2$, above which the excitation energies are overestimated. It should be noted that these states are expected to be quite mixed, which might cause a difficulty for the model. The wave functions of the states for band TiP1 are illustrated in Fig. 10. The $13/2^-$ band-head has about 70% contribution from the
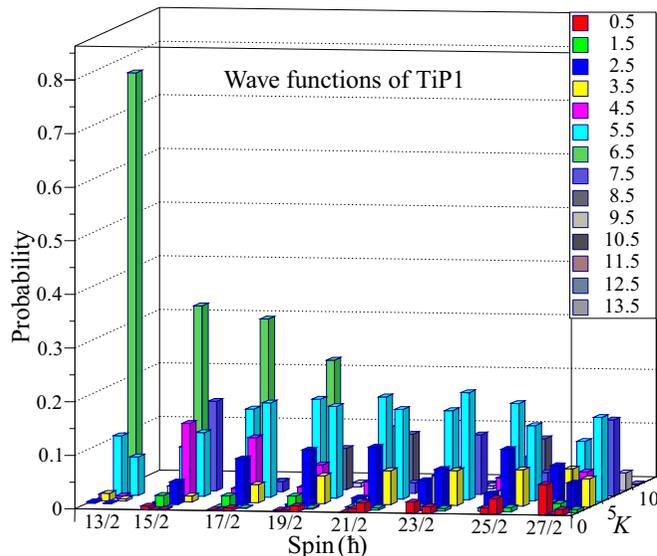
FIG. 10. The same as Fig. 9, but for band TiP1.
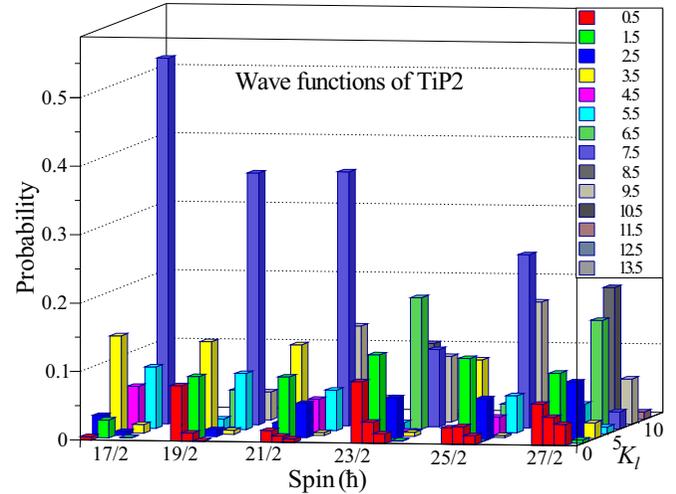
FIG. 11. The same as Fig. 9, but for band TiP2.

basis function #18 (mainly $\nu h_{11/2}[514]\frac{9}{2}$) with $K_l = 13/2$ and $R_l = 2$, shown in green. This basis function is of the type [9/2, 13/2], suggesting a rotational angular momentum along the long axis of $R_l = 2$, see Fig. 7. The four low-spin states of band TiP1 have largest contribution from this basis function, but at highest spins the wave functions of the states represent a mixture of multiple basis functions with different nature. Therefore TiP1 is associated mostly with [9/2, 13/2] nature, even if the states with $I > 19/2$ are very mixed.

Figure 11 illustrates the contribution of wave functions for the states in TiP2 band. The $17/2^-$ state has largest contribution from the basis function #19 with $K_l = 15/2$ and $R_l = 2$, shown in blue. This basis function is of type [11/2, 15/2], suggesting that the $\Omega_l = 11/2$ orbital is involved, see Fig 7. This $\nu h_{11/2}[505]\frac{11}{2}$ orbital is important for all states of TiP2 and is dominant for the three low-spin states, which were identified experimentally. Other basis functions, in particular corresponding to orbitals with lower Ω_l are also present, reflecting the partial misalignment of the angular momentum of the odd neutron. Therefore band TiP2 in the observed spin range is associated with dominant [11/2, 15/2] nature. In addition, one can also notice that the excitation energy of the states in band TiP2 are reproduced very well by the QTR model, see Fig. 8.

To further refine the understanding of the properties of the bands in ^{135}Nd, the calculated reduced transition probabilities were compared with the experimental data. Figure 12(a) shows the $B(M1, I \rightarrow I - 1)/B(E2)_{\text{in}}$ ratios for intra-band transitions of D1 (blue) and interconnecting transitions of bands TiP1 and D1 (red). The calculations are in excellent agreement with the experimental data. The $B(E2, I \rightarrow I - 1)/B(E2)_{\text{in}}$ ratios for the intraband transitions in D1 and interconnecting transitions of bands TiP1 and D1 are displayed in Fig. 12(b). There is very good agreement for interband transitions linking the bands D1 and TiP1, while the calculations slightly overestimate these ratios for the intraband transitions in band D1. In general, however, the agreement between calculations and experimental data is very good for both $B(M1, I \rightarrow I - 1)/B(E2)_{\text{in}}$ and $B(E2, I \rightarrow I - 1)/B(E2)_{\text{in}}$
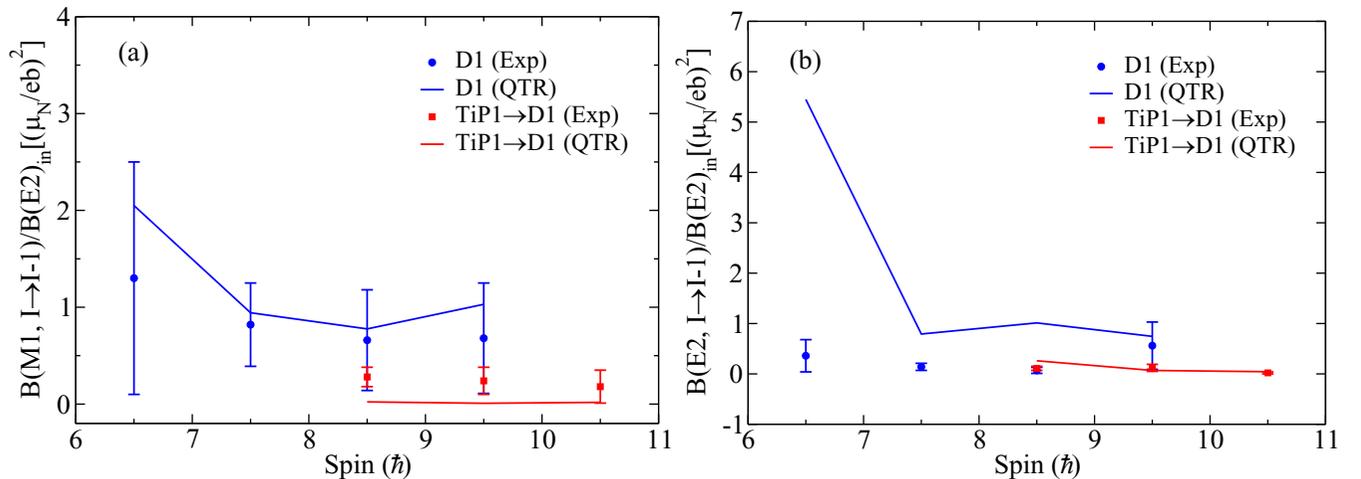
FIG. 12. Comparison of the experimental and calculated $B(M1, I \to I-1)/B(E2)_{in}$ and $B(E2, I \to I-1)/B(E2)_{in}$ ratios for the intraband transitions of band D1 and for the transitions between bands TiP1 and D1.

ratios, as shown in Fig. 12 and supports the proposed interpretation.

IV. SUMMARY

In summary, two low-lying yrare bands in ^{135}Nd have been observed which are connected to band D1 by many $M1$ and $E2$ transitions. Spins and parities of the TiP bands have been firmly determined based on R_{DCO}, R_{ac} and polarization measurements. Results obtained from QTR calculations are in good agreement with experimental data. The bands have therefore been assigned as tilted precession bands with $\nu h_{11/2}$ nature. This result opens a new insight into the interpretation of nuclei with triaxial deformation and adds a new dimension to the description of rotational bands in odd-A nuclei.

APPENDIX A: COMPARISON BETWEEN THE TIP AND WOBBLING BANDS

The similarities and the differences between TiP and wobbling bands are highlighted in Fig. 13. Both TiP and wobbling have been studied in Ref. [48] and correspond to precession of the total angular momentum around a certain axis. For instance in even-even nuclei where the triaxial nucleus rotates mainly around the intermediate axis, several rotational bands are produced. For the yrast band the total angular momentum precesses around the intermediate axis, shown as $I(b_0)$ in Fig. 13(a), while for the excited bands similar precession is present but at a larger tilt angle, for instance $I(b_1)$ and $I(b_2)$ in Fig. 13(a). In Fig. 13(b) the precession of the total angular momentum for an odd-mass nucleus with transverse coupling of the angular momenta of the odd nucleon, j, and of the core, R, is illustrated assuming that the odd nucleon is frozen. In this case the total angular momentum precesses around the axis of j. Each excited band corresponds to a precession of the total angular momentum at a larger tilt angle with respect to that axis. Such precession is possible for a limited spin range only, because beyond a critical spin, I_c, the total angular momentum tilts away to precess around a tilted axis as illustrated by the dashed-line circles in Fig. 13(c), forming new bands with $\Delta I = 1$ nature, see Fig. 13(e).

Fixing the angular momentum of the odd nucleon in a direction perpendicular to the largest rotational angular momentum neglects the Coriolis interaction. Freeing the odd nucleon allows its realignment and decreases the value of I_c, and therefore decreases the spin range where the total angular momentum precesses around the intermediate axis.

The tilted precession of the total angular momentum along the intermediate axis, Fig. 13(a), or along the perpendicular axis, Fig. 13(b) was approximated with wobbling, where the extra tilt of each excited band was caused by an
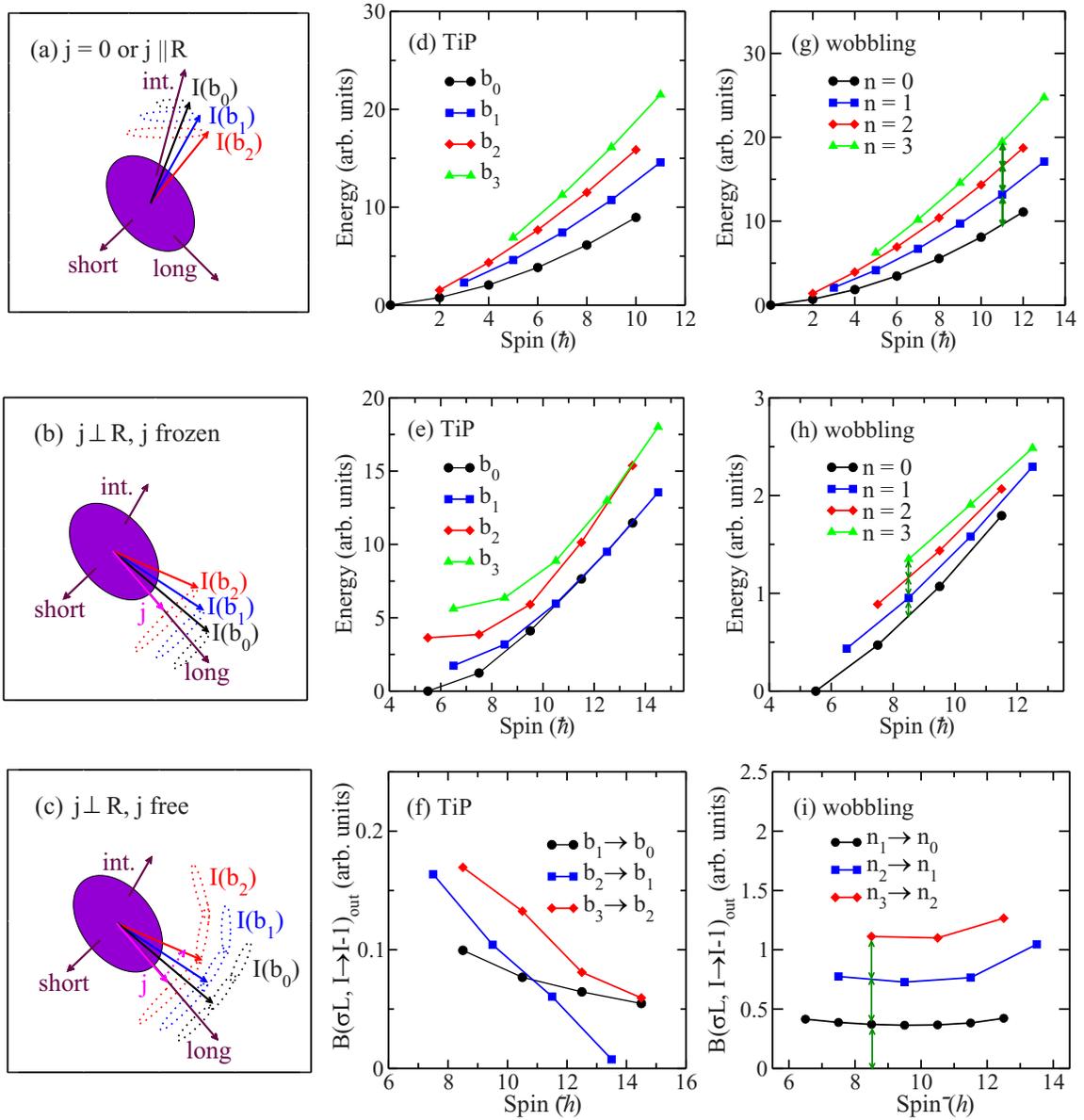
FIG. 13. (a)–(c) show a schematic illustration of the precession of the total angular momentum for: (a) even-even nuclei with no odd nucleon ($j = 0$) or with odd nucleon aligned along the intermediate axis ($j \parallel R$); (b) odd-mass nuclei with an odd nucleon aligned along the short or long nuclear axis, ($j \perp R$), where j is frozen, and (c) odd-mass nuclei as in (b) but where the odd nucleon is free. (d) and (g) illustrate the excitation energies of the TiP and wobbling bands, respectively, for an angular momentum coupling as shown in (a). (e), and (h) show the excitation energies corresponding to a coupling as shown in (b). (f), and (i) illustrate the reduced transition probabilities $B(\sigma L, I \rightarrow I - 1)_{\text{out}}$, where σ stands for M (or E) and L stands for 1 (or 2) for transitions linking two consecutive bands, for instance b_2 to b_1 for TiP bands or $n = 2$ to $n = 1$ for wobbling bands. The green double arrows in (g)–(i) highlight the expected phonon quantization.

excitation of an wobbling phonon [33]. This description results in quantization of the excitation energies and reduced transition probabilities of the excited bands, as illustrated in Fig. 13(g)–13(i). Following the phonon nature of the wobbling approximation, the excitation energy is proportional to the number of the excited phonons n, see panels (g) and (i) for longitudinal and transverse angular momenta couplings, respectively. As a result of the phonon nature of the wobbling bands both $B[M1, I(n) \rightarrow I - 1(n - 1)]$ and $B[E2, I(n) \rightarrow I - 1(n - 1)]$ are proportional to n, and therefore the transi-

tion probabilities for the excited bands increase linearly with n, as illustrated in Fig. 13(i).

Wobbling was introduced for frozen angular momentum of the odd nucleon in an odd-mass nucleus. This approach considers collective excitations only, which reflects the collective nature of the wobbling motion. A more realistic description is however obtained assuming that the angular momentum of the odd nucleon is free to align under the effect of the Coriolis force. This introduces non-collective contributions which cannot be associated with wobbling excitations. Such

more general description can be done however within the QTR mode. The angular momentum in such bands are generated by both collective rotation of the core and by the re-alignment of the odd nucleon. The re-alignment introduces additional discrepancies between the features of the TiP and wobbling bands based on frozen approximation which are not illustrated in Fig. 13.

APPENDIX B: COMMENTS ON THE DIFFERENCE BETWEEN PRM [7] AND PRESENT QTR CALCULATIONS

The important differences between the PRM [7] and the present QTR calculations are that: (i) the PRM can be carried out for multi-particle configurations while the present QTR can be applied for up to two valence particles; (ii) the PRM does not include pairing as it is very complicated to incorporate it for multiparticle configuration. According to our knowledge there are only two many-particle PRM codes available at present [64] and [65,66], and they both do not include pairing. Contrary to that, the QTR code includes the pairing interaction.

Both PRM and QTR models are based on the same physics, both of them describe coupling of valence nucleon(s) to a rotating core, therefore they both describe the same general phenomenon, the rotation of a rigid triaxial nucleus with valence nucleons. Due to the inclusion of pairing, QTR is more appropriate when describing low-spin states where the impact of pairing is largest. At high spins, where several nucleon pairs are broken, the pairing effect has smaller magnitude. In Ref. [7] we have used PRM to describe the high-spin states in ^{135}Nd, and in addition we have also used it for the yrast low-spin band, D1. While the use of PRM without pairing is not optimal for low-spin states, the pairing interaction in general affects the excited bands at low spins more significantly than the yrast band, as will be discussed below.

The rotational model considers a coupling of two types of excitations, of single-particle type which describes the single-particle excitations of the odd nucleon, and of collective type which describes the three-dimensional rotation of a triaxial nucleus. The calculated rotational bands correspond in general to a mixture of these two different types of excitation. The yrast rotational band can be described, in a simplified way, as a coupling of the lowest-energy single-particle orbital to a rotation around the intermediate nuclear axis (within the irrotational flow description the moment of inertia around the intermediate axis is largest, so rotation around the intermediate axis is favorite and produces the yrast rotational band). The excited bands have a more complex structure involving a diverse mixture of competing single-particle and collective excitations.

The collective excitations are governed by the shape parameters, the quadrupole deformation and the triaxiality, and the moments of inertia. In both the present QTR and previous PRM calculations in Ref. [7] we use the irrotational flow model for the moments of inertia and the same deformation parameters.

The single-particle excitations strongly depend on the relative energy of the calculated single-particle orbitals near the Fermi level. For the same nuclear deformation, the difference
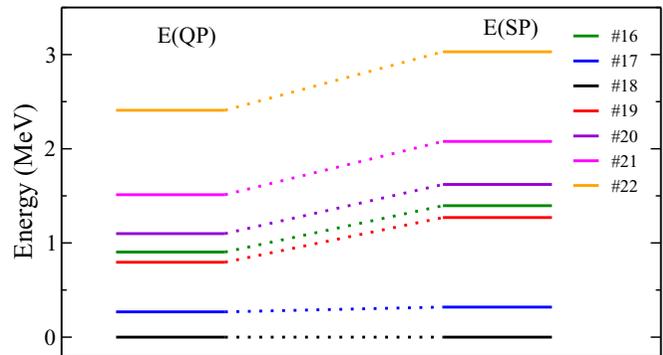

FIG. 14. Calculated energies of the negative-parity quasiparticle orbitals E(QP), and single-particle orbitals E(SP), near the Fermi level of ^{135}Nd.

between the relative energies of the single-particle (PRM) and the quasiparticle (QTR) orbitals is caused by the pairing interaction. It is well known that for an odd-mass nucleus the pairing decreases the relative spacing of the single-particle levels, therefore the quasiparticle orbitals lie closer to each other than the single-particle ones. In the present case the energies of the orbitals near the Fermi level calculated with pairing (QP) and without pairing (SP) are shown in Fig. 14. The Fermi level is near the orbital #18. One can see that neglecting the pairing interaction raises the relative excitation energy of the single-particle excitations. We are showing in Fig. 15 calculations with input parameters identical to those of the QTR calculations shown in Fig. 8 of the main manuscript, except that the pairing is excluded. It is clear that neglecting the pairing worsens the agreement between experimental data and calculations for both excited bands, TiP1 and TiP2, while it has only minor effect on the yrast band, D1.

The QTR calculations presented in this work were carried out with the same parameters for the quadrupole deformation and triaxiality as our previous study in Ref. [7]. The choice of the deformation parameters was based on the prediction by our CDFT calculations [7]. The observed energy stagger-
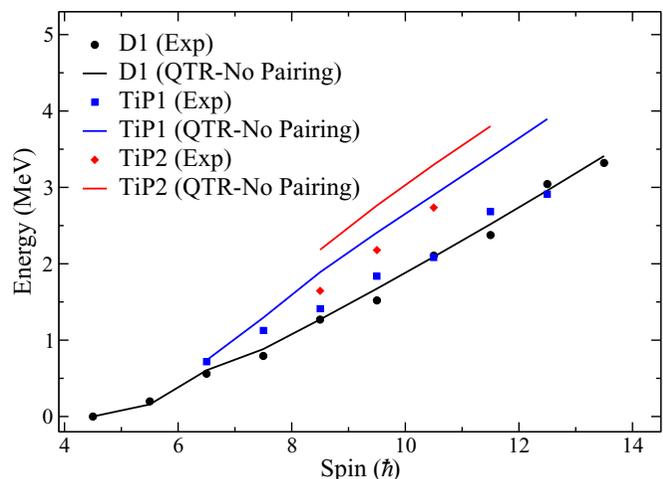

FIG. 15. The calculated excitation energies of the $h_{11/2}$ negative-parity bands in ^{135}Nd where the pairing is excluded.

ing in D1 supported a large triaxiality. Here, experimental data for two new bands, TiP1 and TiP2, are presented. The new results, in particular the $B(E2; \text{TiP1} \to \text{D1})$ reduced transition probabilities, carry direct information on whether the excited band is generated by predominantly collective or noncollective excitation with respect the yrast band, and depends strongly on the competition of collective and noncollective type of contributions to the wave function of the excited band. The present QTR calculations using the

deformation parameters from our previous work, Ref. [7], reproduce the $B(E2)_{\text{out}}/B(E2)_{\text{in}}$ ratios for TiP1 very well: the calculated values in the range of 0.26 and 0.04 compare well with the experimental values in the range of 0.12 and 0.02. Such good agreement with the new experimental data, without a need to modify the previously used deformation parameters, was not anticipated and suggests that the predicted by CDFT nuclear deformation parameters are reliable and trustworthy.

---

[1] P. Möller, R. Bengtsson, B. G. Carlsson, P. Olivius, and T. Ichikawa, Phys. Rev. Lett. **97**, 162502 (2006).
[2] S. Frauendorf and J. Meng, Nucl. Phys. A **617**, 131 (1997).
[3] S. Guo *et al.*, Phys. Lett. B **807**, 135572 (2020).
[4] C. M. Petrache *et al.*, Phys. Rev. C **94**, 064309 (2016).
[5] A. D. Ayangeakaa *et al.*, Phys. Rev. Lett. **110**, 172504 (2013).
[6] S. Zhu *et al.*, Phys. Rev. Lett. **91**, 132501 (2003).
[7] B. F. Lv *et al.*, Phys. Rev. C **100**, 024314 (2019).
[8] S. Mukhopadhyay *et al.*, Phys. Rev. Lett. **99**, 172501 (2007).
[9] C. M. Petrache *et al.*, Phys. Rev. C **97**, 041304(R) (2018).
[10] C. M. Petrache *et al.*, Eur. Phys. J. A **56**, 208 (2020).
[11] C. M. Petrache *et al.*, Phys. Rev. C **86**, 044321 (2012).
[12] T. Marchlewski *et al.*, Acta Phys. Pol. B **46**, 689 (2015).
[13] K. Selvakumar *et al.*, Phys. Rev. C **92**, 064307 (2015).
[14] E. Grodner *et al.*, Phys. Lett. B **703**, 46 (2011).
[15] E. Grodner *et al.*, Phys. Rev. Lett. **97**, 172501 (2006).
[16] X. Wu *et al.*, Plasma Sci. Technol. **14**, 526 (2012).
[17] J. Ndayishimye *et al.*, Phys. Rev. C **100**, 014313 (2019).
[18] P. L. Masiteng *et al.*, Phys. Lett. B **719**, 83 (2013).
[19] P. L. Masiteng *et al.*, Eur. Phys. J. A **50**, 119 (2014).
[20] P. L. Masiteng *et al.*, Eur. Phys. J. A **52**, 28 (2016).
[21] T. Roy *et al.*, Phys. Lett. B **782**, 768 (2018).
[22] E. Lawrie *et al.*, Eur. Phys. J. A **45**, 39 (2010).
[23] I. Kuti *et al.*, Phys. Rev. Lett. **113**, 032501 (2014).
[24] J. A. Alcántara-Núñez *et al.*, Phys. Rev. C **69**, 024317 (2004).
[25] J. Timár *et al.*, Phys. Lett. B **598**, 178 (2004).
[26] Y. X. Luo *et al.*, Phys. Rev. C **69**, 024315 (2004).
[27] J. Timár *et al.*, Phys. Rev. C **76**, 024307 (2007).
[28] C. Y. He *et al.*, Plasma Sci. Technol. **14**, 518 (2012).
[29] C. Liu *et al.*, Phys. Rev. Lett. **116**, 112501 (2016).
[30] S. Y. Wang *et al.*, Phys. Lett. B **703**, 40 (2011).
[31] B. W. Xiong and Y. Y. Wang, At. Data Nucl. Data Tables **125**, 193 (2019).
[32] A. Bohr and B. R. Mottelson, *Nuclear Structure*, Vol. I (Benjamin, New York, 1975).
[33] S. Frauendorf and F. Dönau, Phys. Rev. C **89**, 014322 (2014).
[34] P. Bringel *et al.*, Eur. Phys. J. A **24**, 167 (2005).
[35] S. W. Ødegård *et al.*, Phys. Rev. Lett. **86**, 5866 (2001).
[36] D. R. Jensen *et al.*, Phys. Rev. Lett. **89**, 142503 (2002).
[37] G. Schönwaßer *et al.*, Phys. Lett. B **552**, 9 (2003).
[38] H. Amro *et al.*, Phys. Lett. B **553**, 197 (2003).
[39] D. J. Hartley *et al.*, Phys. Rev. C **80**, 041304(R) (2009).
[40] J. Timár *et al.*, Phys. Rev. Lett. **122**, 062501 (2019).
[41] J. T. Matta, *et al.*, Phys. Rev. Lett. **114**, 082501 (2015).
[42] N. Sensharma *et al.*, Phys. Lett. B **792**, 170 (2019).

[43] Q. B. Chen, S. Frauendorf, and C. M. Petrache, Phys. Rev. C **100**, 061301(R) (2019).
[44] B. Subhagata *et al.*, Eur. Phys. J. A **55**, 159 (2019).
[45] K. Tanabe and K. Sugawara-Tanabe, Phys. Rev. C **95**, 064315 (2017).
[46] K. Tanabe and K. Sugawara-Tanabe, Phys. Rev. C **97**, 069802 (2018).
[47] N. Sensharma *et al.*, Phys. Rev. Lett. **124**, 052501 (2020).
[48] E. A. Lawrie, O. Shirinda, and C. M. Petrache, Phys. Rev. C **101**, 034306 (2020).
[49] J. Meyer-Ter-Vehn, Nucl. Phys. A **249**, 111 (1975).
[50] W. F. Piel, C. W. Beausang, D. B. Fossan, L. Hildingsson, and E. S. Paul, Phys. Rev. C **35**, 959 (1987).
[51] P. Rahkila, Nucl. Instrum. Methods Phys. Res. A **595**, 637 (2008).
[52] B. F. Lv *et al.*, Phys. Rev. C **98**, 044304 (2018).
[53] D. Radford, Nucl. Instrum. Methods Phys. Res. A **361**, 297 (1995).
[54] D. Radford, Nucl. Instrum. Methods Phys. Res. A **361**, 306 (1995).
[55] A. Krämer-Flecken, T. Morek, R. M. Lieder, W. Gast, G. Hebbinghaus, H. M. Jäger, and W. Urban, Nucl. Instrum. Methods Phys. Res. A **275**, 333 (1989).
[56] C. J. Chiara *et al.*, Phys. Rev. C **75**, 054305 (2007).
[57] A. Herzáň *et al.*, Phys. Rev. C **92**, 044310 (2015).
[58] K. Starosta *et al.*, Nucl. Instrum. Methods Phys. Res. A **423**, 16 (1999).
[59] P. B. Semmes and I. Ragnarsson, in *Proceedings of the International Conference on High-Spin Physics and Gamma-Soft Nuclei, Pittsburg*, edited by J. X. Saladin, R. A. Sorenson, and C. M. Vincent (World Scientific, Singapore, 1991), p. 500; in *Future Directions in Nuclear Physics with 4π Gamma Detection Systems of the New Generation*, edited by J. Dudek and B. Haas, AIP Conf. Proc. No. 259 (AIP, Woodbury, NY, 1992), p. 566.
[60] J. Allmond and J. Wood, Phys. Lett. B **767**, 226 (2017).
[61] P. Ring and P. Schuck, *The Nuclear Many-Body Problem* (Springer Science & Business Media, 2004).
[62] E. M. Beck *et al.*, Phys. Rev. Lett. **58**, 2182 (1987).
[63] T. Klemme *et al.*, Phys. Rev. C **60**, 034301 (1999).
[64] B. G. Carlsson and I. Ragnarsson, Phys. Rev. C **74**, 011302(R) (2006).
[65] B. Qi, S. Q. Zhang, J. Meng, S. Y. Wang, and S. Frauendorf, Phys. Lett. B **675**, 175 (2009).
[66] Q. B. Chen, B. F. Lv, C. M. Petrache, and J. Meng, Phys. Lett. B **782**, 744 (2018).